Article

Structure

Structural Basis for Dodecameric Assembly States and Conformational Plasticity of the Full-Length AAA+ ATPases Rvb1·Rvb2

Graphical Abstract

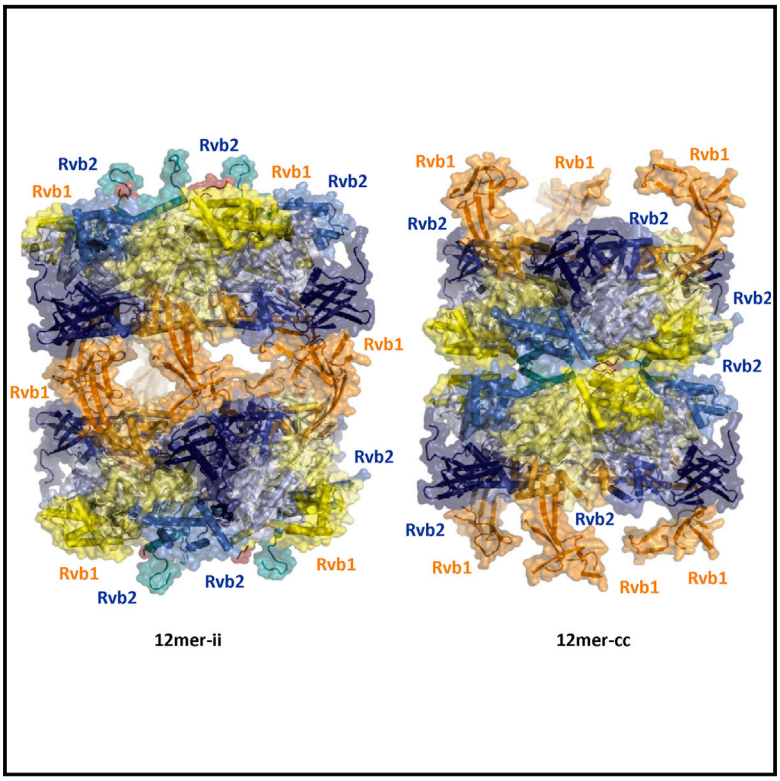

Authors

Kristina Lakomek, Gabriele Stoehr, ..., Monika Schmailzl, Karl-Peter Hopfner

Correspondence

hopfner@genzentrum.lmu.de

In Brief

Structures of full-length Rvb1(ATP)-Rvb2(*apo*) and Rvb1(ADP)-Rvb2(ADP) heterohexamers, described by Lakomek et al., exhibit interconnected structural rearrangements and unequal places of the OB folds of Rvb1 and Rvb2 relative to the AAA+ core. ATP binding but not hydrolysis in Rvb1 is required for Rvb2's ATPase activity and vice versa.

Highlights

- Full-length Rvb1-Rvb2 heterohexamer crystal structures provide dodecamer framework
- OB-fold domains of Rvb1 and Rvb2 occupy unequal places relative to AAA+ core
- Rvb1(ATP)Rvb2(*apo*) and Rvb1(ADP)Rvb2(ADP) structures reveal coupled rearrangements
- ATP binding but not hydrolysis by neighbor subunit is required for ATPase activity

Accession Numbers

4WVY
4WW4

Lakomek et al., 2015, Structure *23*, 483–495
March 3, 2015
http://dx.doi.org/10.1016/j.str.2014.12.015

Structure
Article

Structural Basis for Dodecameric Assembly States and Conformational Plasticity of the Full-Length AAA+ ATPases Rvb1·Rvb2

Kristina Lakomek,[1] Gabriele Stoehr,[1] Alessandro Tosi,[1] Monika Schmailzl,[1] and Karl-Peter Hopfner[1,2,*]
[1]Department of Biochemistry, Gene Center of the Ludwig-Maximilians University Munich, 81377 Munich, Germany
[2]Center for Integrated Protein Sciences, Ludwig-Maximilians University Munich, Feodor-Lynen-Str. 25, 81377 Munich, Germany
*Correspondence: hopfner@genzentrum.lmu.de
http://dx.doi.org/10.1016/j.str.2014.12.015

SUMMARY

As building blocks of diverse macromolecular complexes, the AAA+ ATPases Rvb1 and Rvb2 are crucial for many cellular activities including cancer-related processes. Their oligomeric structure and function remain unclear. We report the crystal structures of full-length heteromeric Rvb1·Rvb2 complexes in distinct nucleotide binding states. *Chaetomium thermophilum* Rvb1·Rvb2 assemble into hexameric rings of alternating molecules and into stable dodecamers. Intriguingly, the characteristic oligonucleotide-binding (OB) fold domains (DIIs) of Rvb1 and Rvb2 occupy unequal places relative to the compact AAA+ core ring. While Rvb1's DII forms contacts between hexamers, Rvb2's DII is rotated 100° outward, occupying lateral positions. ATP was retained bound to Rvb1 but not Rvb2 throughout purification, suggesting nonconcerted ATPase activities and nucleotide binding. Significant conformational differences between nucleotide-free and ATP-/ADP-bound states in the crystal structures and in solution suggest that the functional role of Rvb1·Rvb2 is mediated by highly interconnected structural switches. Our structures provide an atomic framework for dodecameric states and Rvb1·Rvb2's conformational plasticity.

INTRODUCTION

Rvb1 and Rvb2 (*RuvB*-like, also denoted RuvBL1/RuvBL2, Pontin/Reptin, and TIP48/TIP49) belong to the classical AAA clade of the AAA+ protein superfamily (*A*TPases *a*ssociated with diverse cellular *a*ctivities). Rvb1 and Rvb2 are crucial for a plethora of cellular processes and part of diverse macromolecular machines. Although Rvb1 and Rvb2 orthologs are essential in a variety of species, their exact molecular functions are still unclear. Their roles vary from transcriptional regulation and DNA repair to telomerase assembly and mitotic spindle formation and, via interaction with oncogenic transcription factors, also concern cancer-related processes (reviewed in Huber et al., 2008; Huen et al., 2010; Jha and Dutta, 2009; Nano and Houry, 2013; Rosenbaum et al., 2013). Rvb1 and Rvb2 interact with oligomers of the transcription factor Yin Yang 1 (López-Perrote et al., 2014) and the histone acetyltransferase TIP60 complex (Ikura et al., 2000) and are integral components of the large chromatin remodelers INO80 and SWR1 (Krogan et al., 2003; Shen et al., 2000). Rvb1 and Rvb2 also participate in the assembly of complexes containing the *p*hosphatidyl*i*nositol-*3*-*k*inase (PI3K)-like *k*inases (PIKKs) ATM, ATR, mTOR, and SMG-1 (reviewed in Izumi et al., 2012). They occur in the R2TP (*R*vb1-*R*vb2-*T*ah1-*P*ih1) complex (reviewed in Kakihara and Houry, 2012) and are implicated in snoRNP biogenesis (reviewed, e.g., in Nano and Houry, 2013).

Rvb1 and Rvb2 share the same tripartite fold composed of domains DI and DIII forming the ubiquitous AAA+ ATPase core and an Rvb1/Rvb2-specific insertion domain (DII), which harbors an oligonucleotide-binding (OB) fold. ATP plays an important functional role (Ammelburg et al., 2006; Snider and Houry, 2008; Wendler et al., 2012; Afanasyeva et al., 2014). ATP hydrolysis activity can be detected for both Rvb1 or Rvb2, albeit weak (as analyzed, e.g., in Gorynia et al., 2011; Gribun et al., 2008; Ikura et al., 2000; Kanemaki et al., 1999; Makino et al., 1999; Matias et al., 2006; Papin et al., 2010; Puri et al., 2007; Rottbauer et al., 2002; and comprehensively reviewed on www.gref-bordeaux.fr/fr/node/303). In vivo, Rvb1's and Rvb2's ATPase activities are required for telomerase assembly (Venteicher et al., 2008) and snoRNA production (King et al., 2001), respectively.

Rvb1 has been shown to bind single-stranded (ss) and double-stranded (ds) DNA as well as ssRNA, mediated by its DII domain (Matias et al., 2006). Existence of additional helicase activity is ambiguous. DNA unwinding activity has been demonstrated in vitro (Gorynia et al., 2011; Gribun et al., 2008; Kanemaki et al., 1999; Makino et al., 1999; Papin et al., 2010). At least in the human proteins, DII seems to autoinhibit the DNA helicase activity and to regulate the ATPase function (Gorynia et al., 2011). Whether, for example, INO80's 3′→5′ helicase activity (Shen et al., 2000) is executed directly by the Rvbs is not clear. The presence of Rvb1/Rvb2 is required for INO80's remodeling activity in yeast (Jonsson et al., 2004). For human INO80, the need is still under debate (Chen et al., 2013). In contrast, TIP60's helicase activity is not attributable to Rvb1/Rvb2 (Ikura et al., 2000).

AAA+ ATPases typically form oligomeric rings, with the ATPase site formed in the interface of two adjacent protomers. It is unclear whether Rvb1 and Rvb2 form homohexamers or heterohexamers and, if so, whether these are composed of alternating Rvb1 and Rvb2, and whether two hexamers assemble

Table 1. Data Collection and Refinement Statistics

	*ct*Rvb1(ADP)-*ct*Rvb2(ADP)	*ct*Rvb1(ATP)-*ct*Rvb2(*apo*)
Data collection		
Beamline	ID29, ESRF, France	SLS, Switzerland
Detector	PILATUS 6M-F	PILATUS 6M
Wavelength (Å)	0.972386	0.91889
Space group	R32 : H	R32 : H
Cell dimensions		
a, *b*, *c* (Å)	206.848, 206.848, 137.441	210.35, 210.35, 137.14
Resolution (Å)	75.04–2.94 (3.10–2.94)	34.50–3.64 (3.84–3.64)
R_{pim} [a] (%)	5.2 (43.2)	3.5 (28.7)
$I/\sigma(I)$	8.3 (1.7)	15.9 (3.9)
Wilson B (Å^2)	70.0	104.4
Completeness (%)	97.4 (96.9)	99.9 (100.0)
Refl. total/unique	103,751/23,417	190,173/13,158
Redundancy	4.4 (3.2)	14.5 (14.3)
Software used for data processing	MOSFLM/SCALA	MOSFLM/SCALA
Refinement		
Resolution (Å)	64.16–2.94 (3.07–2.94)	33.69–3.64 (3.93–3.64)
No. of reflections	23,414	13,156
R_{work} (%)	19.75	22.14
R_{free} [b] (%)	22.31	25.06
No. of atoms	6,617	6,456
Protein	6,535	6,425
Ligand/ion	68	31
Water	14	–
B factors (Å^2)	99.8	143.7
Protein	100.0	143.7
Ligand/ion	80.1	143.8
Water	56.4	–
Solvent content (%)	53.8	55.2
Rmsd bond length (Å)	0.008	0.008
Rmsd bond angle (°)	1.06	1.00
Ramachandran plot, favored/disallowed (%)	96/0	95/0
Coordinate error (Å)[c]	0.55	1.13
PDB code	4WW4	4WVY

Values in parentheses are for the highest-resolution shell.

[a] $R_{pim} = \sum_{j=1}^{n} |I_j(hkl) - \langle I(hkl)\rangle| / \sum_{hkl}\sum_{j} I_j(hkl)$.

[b] R_{free} factor calculated for 5% randomly chosen reflections not included in the refinement.

[c] Coordinate error estimated from Luzzati plot (Å).

into a dodecamer. A variety of structural studies addressed the oligomeric state of Rvbs by size exclusion chromatography (SEC) and analytical ultracentrifugation (AUC) (Niewiarowski et al., 2010) or electron microscopy (EM) experiments. The latter have yielded 2D projections of hexameric rings (Cheung et al., 2010b; Gribun et al., 2008) and 3D EM structures of Rvb1·Rvb2 dodecamers from *Saccharomyces cerevisiae* (cryo, 13 Å) (Torreira et al., 2008) or human (Puri et al., 2007; López-Perrote et al., 2012). Still, the resolution of these data does not allow positioning of Rvb1 and Rvb2 subunits. Crystal structures, on the contrary, revealed both homo- and heterohexameric rings of the human proteins (Matias et al., 2006; Petukhov et al., 2012; Gorynia et al., 2011). Experimental as well as computational studies confirmed the coexistence of a number of different assembly forms in vitro (Niewiarowski et al., 2010) and conformational flexibility (Petukhov et al., 2012). Here we provide the structure of a full-length complex of Rvb1 and Rvb2 from the thermophilic fungus *Chaetomium thermophilum* (*ct*Rvb1·*ct*Rvb2). It shows a hexameric ring of alternating Rvb1 and Rvb2 molecules and its assembly into dodecameric states. Intriguingly, the Rvb1/2-specific insertion domains (DII) of Rvb1 and Rvb2 occupy unequal places with respect to the compact AAA+ core ring. We determined two Rvb1/Rvb2 structures that represent distinct nucleotide binding states: ATP/*apo* and ADP/ADP.

Our analysis helps to clarify the structural flexibility of the distinct Rvb1 and Rvb2 domains and their modulation by nucleotide binding and provides a complete atomic framework for *ct*Rvb1·*ct*Rvb2 hexamers and dodecamers.

RESULTS

Crystal Structure of a Full-Length Rvb1·Rvb2 Complex

Structural Determination of ATP/apo and ADP Complexes and Assignment of ctRvb1 and ctRvb2

Rvb1 and Rvb2 from *C. thermophilum* (*ct*Rvb1·*ct*Rvb2) have striking sequence identities (68%) and similarities (86%/85%) to their human orthologs *hs*Rvb1/*hs*Rvb2. *Ct*Rvb1 and *ct*Rvb2 share a sequence identity/similarity of 42%/63% (Figure S1). The crystal structure of the *ct*Rvb1·*ct*Rvb2 complex was obtained without addition of any nucleotide and could be solved by molecular replacement. Initial cycles of building and refinement allowed missing domains to be placed manually and the structure was finally refined to 3.6 Å (Protein Data Bank [PDB] ID 4WVY) (Table 1). The asymmetric unit of the crystal comprises one molecule each of *ct*Rvb1 and *ct*Rvb2 (Figure 1A), an assignment validated by anomalous scattering of inherent sulfur atoms (Figure S2A; Table S1; see Supplemental Information for details). In addition, we derived a 2.9 Å crystal structure of an ADP complex after cocrystallization with ADP-BeF_3 (PDB ID 4WW4) (Table 1). We found an ADP molecule in the nucleotide binding pockets of both *ct*Rvb1 and *ct*Rvb2 (Figure S2B) but no additional density for BeF_3 (see Figure S2B; Supplemental Information).

Domain Organization

Both *ct*Rvb1 and *ct*Rvb2 fold into three domains (DI, DII, and DIII) (Figures 1A and 1B) as described for their human orthologs (PDB IDs 2C9O, 2XSZ, 3UK6) (Gorynia et al., 2011; Matias et al., 2006; Petukhov et al., 2012). Domain DII is composed of an interior region DII_{int} and an OB fold as exterior region DII_{ext}. *Ct*Rvb2 has a C-terminal extension: Pro435-Ser488. A flexible linker of two antiparallel β strands β5 and β11 with a hairpin-like structure connects DI with DII_{ext} (Ile121-Gly134 and His230-Val239 of *ct*Rvb1; split strands β5a, β5b: Ile127-Lys132, Ser135-Glu141 and β11a, β11b: Gln232-Glu236, Val238-Ser242 of

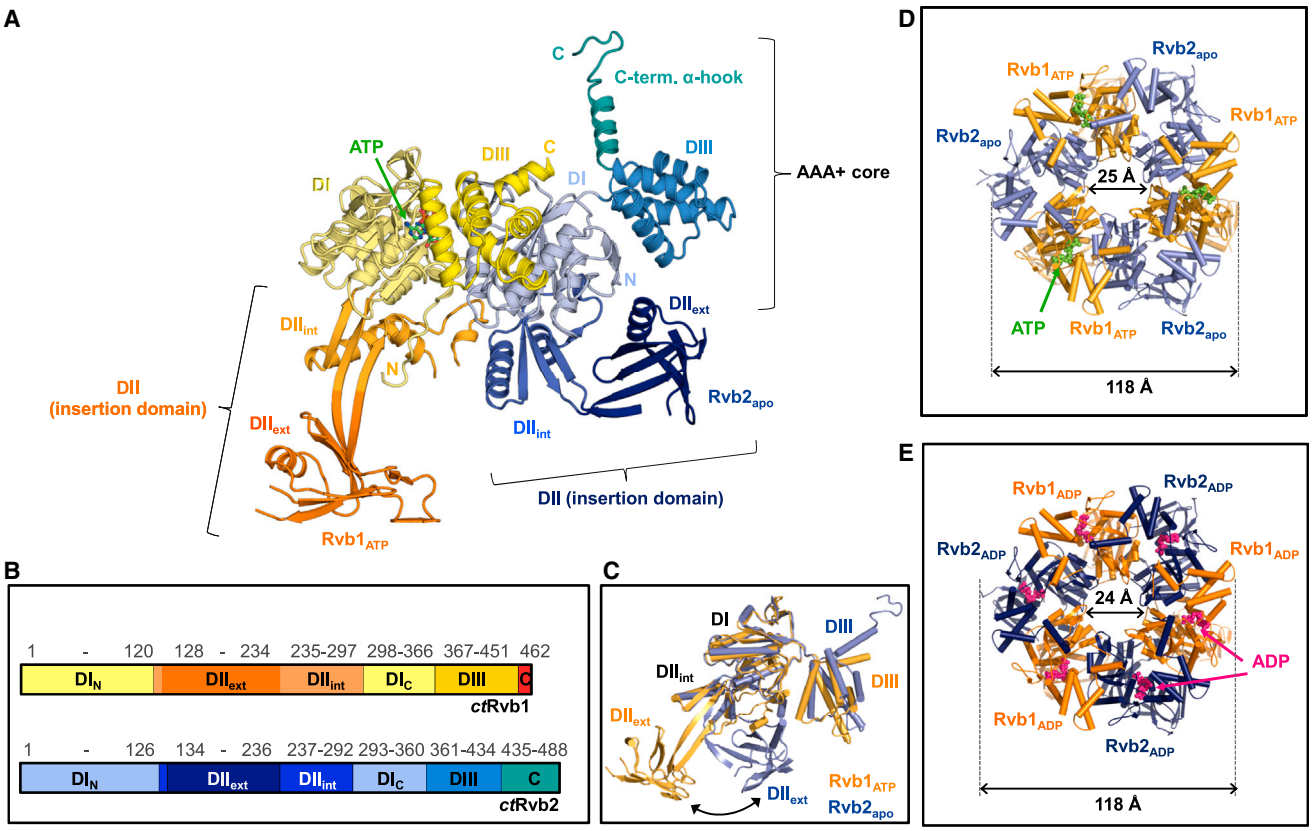

Figure 1. Overall Structure of *ct*Rvb1 and *ct*Rvb2 Monomers and Hexamers in Distinct Nucleotide Binding States

(A) ATP/*apo* *ct*Rvb1·*ct*Rvb2 structure with ATP-bound *ct*Rvb1 and nucleotide-free *ct*Rvb2. Domains DI to DIII are color-coded as labeled.

(B) Schematic of the domain organization with residue numbers of start and end, color-coded as in (A).

(C) *Ct*Rvb1 and *ct*Rvb2 monomers of the ATP/*apo* complex structurally aligned based on DI (see also Figure S1C).

(D and E) Hexameric ring of (D) ATP/apo *ct*Rvb1·*ct*Rvb2 comprising *ct*Rvb1 with bound ATP (green) and nucleotide-free *ct*Rvb2 or (E) the ADP complex with ADP-bound *ct*Rvb1 and ADP-bound *ct*Rvb2 (ADPs in pink), in alternating order, viewed perpendicular to (A) (see also Figures S2E and S2F).

*ct*Rvb2; Figure S1). While the overall fold and conformation of the three individual domains are almost identical for *ct*Rvb1 and *ct*Rvb2, we observe an extreme variance between *ct*Rvb1 and *ct*Rvb2 with regard to the position of their OB folds relative to DI and DIII (Figures 1C and S2C). The β strands that connect DI and DII$_{ext}$ are rather straight and continuous in *ct*Rvb1, whereas the equivalents of *ct*Rvb2 are seriously bent and split into two strands each, resulting in a sharp kink. These strands cross each other at the bend, consistent with the observed DII domain twist toward a lateral position instead of the protruded and more flexible one in *ct*Rvb1 as indicated by elevated atomic B factors (Figure S2D). The dissimilarity between *ct*Rvb1's DII and *ct*Rvb2's swung-out DII becomes particularly important when looking at the biological units of the ATP/*apo* and ADP complexes, which are hexameric rings (Figures 1D, 1E, S2E, and S2F) or dodecamers as described further below.

Structure of the *ct*Rvb1·*ct*Rvb2 Hexamer

Rvb1 and Rvb2 Form a Symmetric Hexameric Ring of 1:1 Stoichiometry

Application of the 3-fold crystallographic axis of the space group R32 generates a hexameric ring of three molecules Rvb1 and Rvb2 each arranged in alternating order (Figures 1D and 1E). It has an outer diameter of 118 Å and a diameter of the central channel of 24–25 Å. The contact areas are mainly composed of hydrophobic residues, but also comprise putative hydrogen-bonding partners. Based on the domains involved, two extensive main *intra*-ring intermolecular contact surfaces of about 2200 Å^2 each can be characterized as "R1(DIII)-R2(DI)" (interface I) and "R2(DIII)-R1(DI)" (interface II) (Figures S3A and S3B; Table S2). The assembly occurs mainly via the AAA+ domains DI and DIII. But interestingly the *ct*Rvb1·*ct*Rvb2 structure reveals that helices and loops of the DIIs are additionally involved to a great extent (Figures 2 and S3). While DII of *ct*Rvb1 in its rather extended conformation points away from the ring, *ct*Rvb2's DII bends in a sharp angle of approximately 100° reaching back to the ring with loop L7 (Ser150-Gly158), leading to a striking difference in DII's position relative to the compact AAA+ ring (Figures 1C, S2C, S2E, S2F, S3C, and S3D). The bending DII position of *ct*Rvb2 is stabilized by Lys183 in α4, which touches back to DI and DIII of the same molecule likely through hydrogen bonds with His26 and Glu376. Importantly, the *ct*Rvb1 or *ct*Rvb2 structures comprise an extended range of residues when compared with other Rvb1/Rvb2 structures, in particular within *ct*Rvb2's DII. New intimate intra-ring contacts between L10 of

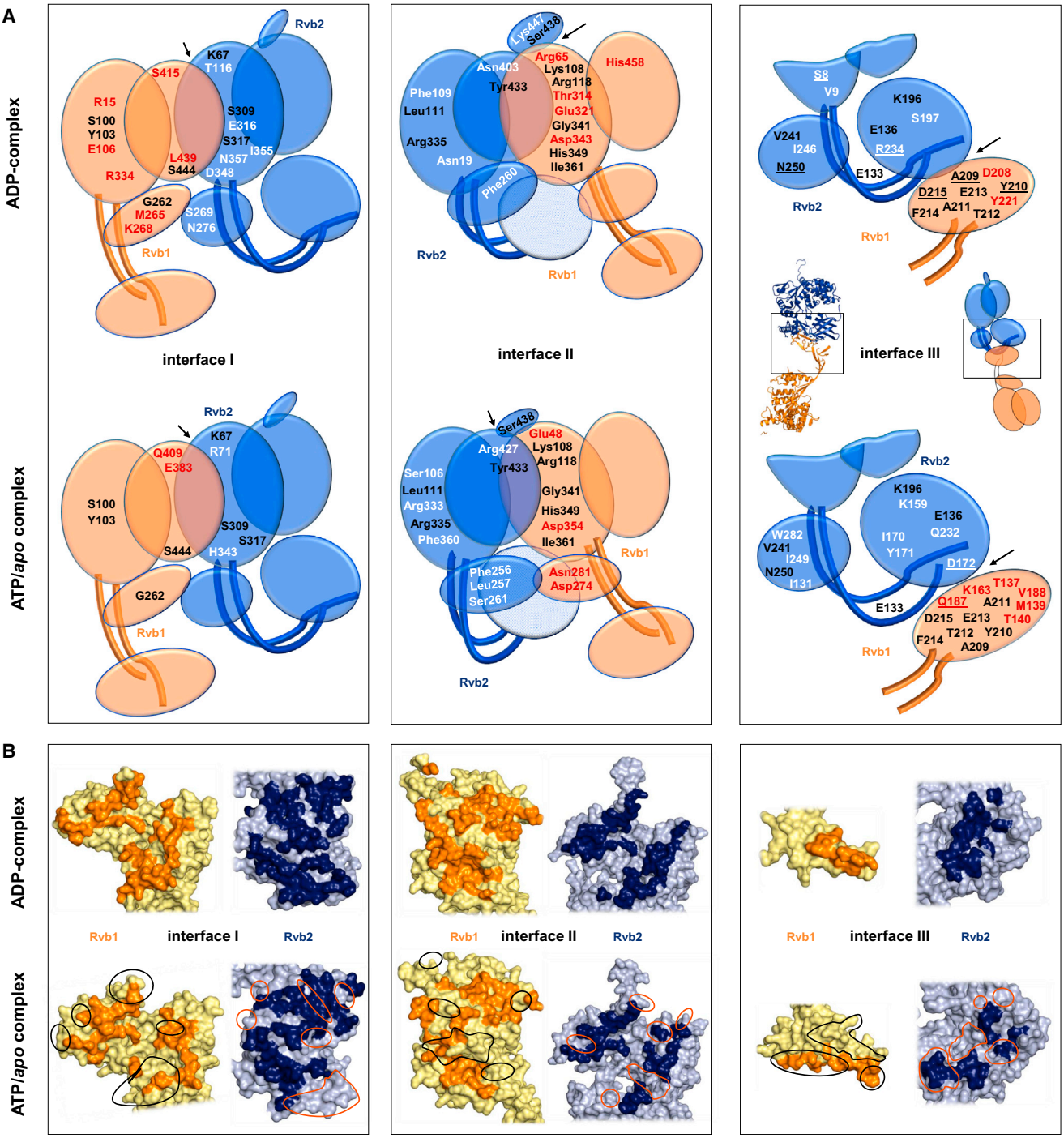

Figure 2. Intermolecular Interactions within DII-DII Dodecamers of *ct*Rvb1·*ct*Rvb2 Complexes in Schematic and Surface Representation

(A) Schematic representation of the residues involved in interactions at the intermolecular interfaces I–III (see Figures S3A and S3B) for the dodecameric ADP- and ATP/*apo* *ct*Rvb1·*ct*Rvb2 complexes (see also Table S2). Domains DI and DIII and *ct*Rvb2's C-terminal part as well as domain regions DII_{int} and DII_{ext} of *ct*Rvb1 and *ct*Rvb2 are depicted as orange and blue ovals, respectively, with the linking hinge of two β strands as thick lines. For clarity, only hydrogen-bonding amino acids are shown for interfaces I and II. For the newly characterized inter-ring interface III instead, all interacting residues are labeled and those forming hydrogen bonds are underlined. Residues that only participate in protein-protein interactions in one of the two crystallized complex states are highlighted in red for *ct*Rvb1 or white for *ct*Rvb2.

(B) Surface regions of *ct*Rvb1 (pale yellow) and *ct*Rvb2 (light blue) with the residues that participate in the formation of the interfaces I–III highlighted in orange and dark blue, respectively. Areas of interaction surfaces that deviate more significantly between the ADP and ATP/*apo* complexes are encircled by black or orange lines.

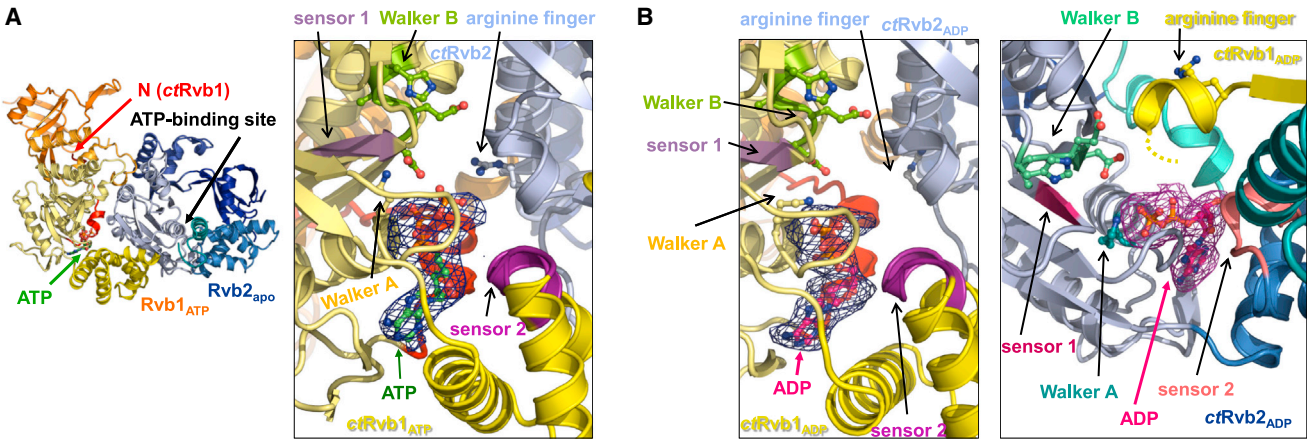

Figure 3. Nucleotide Binding Sites of *ct*Rvb1 and *ct*Rvb2 with F_oF_c Omit Maps for Bound Nucleotides at 3σ

(A) ATP/*apo* complex: overview and close-up onto *ct*Rvb1's active site with bound ATP and color-coded motifs: Walker A (K77), Walker B (DEAH 303–306), sensor 1 (LAS 330–332), sensor 2 (ISLRYC 402–407), and *trans*-arginine finger (R352) of the adjacent *ct*Rvb2.

(B) ADP-complex: close-ups onto the active sites of *ct*Rvb1 (left) and *ct*Rvb2 (right) with one ADP each. Motifs of *ct*Rvb2: Walker A (K83), Walker B (DEVH 298–301), sensor 1 (MAS 325–327), sensor 2 (AGLRYA 396–401), and *trans*-arginine finger (R358) of the neighboring *ct*Rvb1 (see also Figure S2B).

*ct*Rvb2's DII_{int} and α8/α9 in DII_{int}/DII_{ext} of *ct*Rvb1 could be uncovered (Figures S3C and S3D). Decisively, they will affect oligomerization.

Intra-Ring Interfaces I and II

Interface I comprises η3 of *ct*Rvb1 with the adjacent loop L10 (Gly262-Thr273) and α6 of *ct*Rvb2 (Figures 2 and S3C). These contact sites make further interactions leading to an interdependence of domain positions beyond the protomeric border. Interface II comprises a newly identified interaction patch. L10 of *ct*Rvb2's DII_{int} interrelates two helices of *ct*Rvb1 that belong to DII_{int} (α8) or DII_{ext} (α9), respectively, stabilizing this domain arrangement (Figure S3D). At the inner side of the central channel, α12 and α13 of *ct*Rvb2 contact the top surface of *ct*Rvb1's DI. The involved amino acids of *ct*Rvb2 are found in orthologs from yeast to human. Arg437 (in α13) has an extended hydrogen bond network and is stabilized by stacking interactions with Phe429 and Tyr433 of *ct*Rvb2's DIII on both sides. Thereby, the linkage and angle between the two helices are restrained. Arg437 is substituted in some Rvb2 isoforms, which might modify specific functions. Helix α13 is followed by flexible residues that protrude out of the compact ring (Arg448-Val456/Asp457). They adopt a hook-like shape with a short connecting loop. Together with α13 they are referred to as C-terminal α-hook (Figure 1A).

Surface Potential

*Ct*Rvb1's DII bears positive surface patches pointing toward the inside of the central channel. Of note, these surfaces are conserved (Figure S4A) and belong to the most frequently discussed DNA binding regions. Yet, despite additional positively charged areas around the channel's rim at the top and bottom entrance/exit sides, the electrostatic surface potential does not clearly indicate one major nucleic acid binding surface.

Nucleotide Binding Pocket in Distinct States

The nucleotide binding pockets are located at the interfaces between adjacent *ct*Rvb1 and *ct*Rvb2 monomers (Figure 3). The Walker A residue Lys77/83 of *ct*Rvb1/2 in the P-loop (Gly72-Leu80/Gly77-Thr84) is located in DI, while the other conserved motifs for ATP binding, orientation, and hydrolysis belong to DIII: Walker B residues Asp303-Glu304/Asp298-Glu299 and sensor loops 1 (Leu330-Ser332/Met325-Ser327) and 2 (Ile402-Cys407/Ala396-Ala401). Sensor 2 harbors Arg405/399 as a putative *cis*-acting arginine finger (Figure S3E), whereas Arg358/352 of *ct*Rvb1/2 originates from the neighbor molecule as *trans*-arginine finger. The structure obtained without addition of any nucleotide depicts the nucleotide-free state of *ct*Rvb2, while an ATP (but no magnesium ion) was caught in *ct*Rvb1. This structure (PDB ID 4WVY) thus shows a hexameric ring with three occupied nucleotide binding sites (Figure 1D). In sharp contrast, the ADP-complex structure (PDB ID 4WW4) derived from nucleotide cocrystallization experiments shows ADP-binding states of both *ct*Rvb1 and *ct*Rvb2, with all six active sites filled. Obviously, the *ct*Rvb1·*ct*Rvb2 complex can occur in distinct nucleotide binding states without mentionable changes in the characteristic overall dimensions such as outer diameter and central channel of the hexameric ring (Figures 1D and 1E). When comparing domains individually, the two structures are also almost identical. Exceptions concern three β strands of *ct*Rvb1 (β6, β8, and β10) that are entirely included in the ATP/*apo* structure and two helices of *ct*Rvb2 (α1 and η1) present only in the ADP-complex structure.

Dodecameric *ct*Rvb1·*ct*Rvb2 Assemblies

Dodecamers Exist in Solution

SEC and complementary static light-scattering experiments using wild-type and single and double *ct*Rvb1/*ct*Rvb2 Walker A or Walker B mutants in the presence of various nucleotides clearly demonstrate the existence of dodecameric assemblies in solution, independently on an affinity tag (Figure S5A and Supplemental Information).

Two Different Dodecameric Architectures Are Found in the Crystal

When the crystallographic 2-fold axis is deployed onto the hexameric ring, a dodecamer is generated, in which two

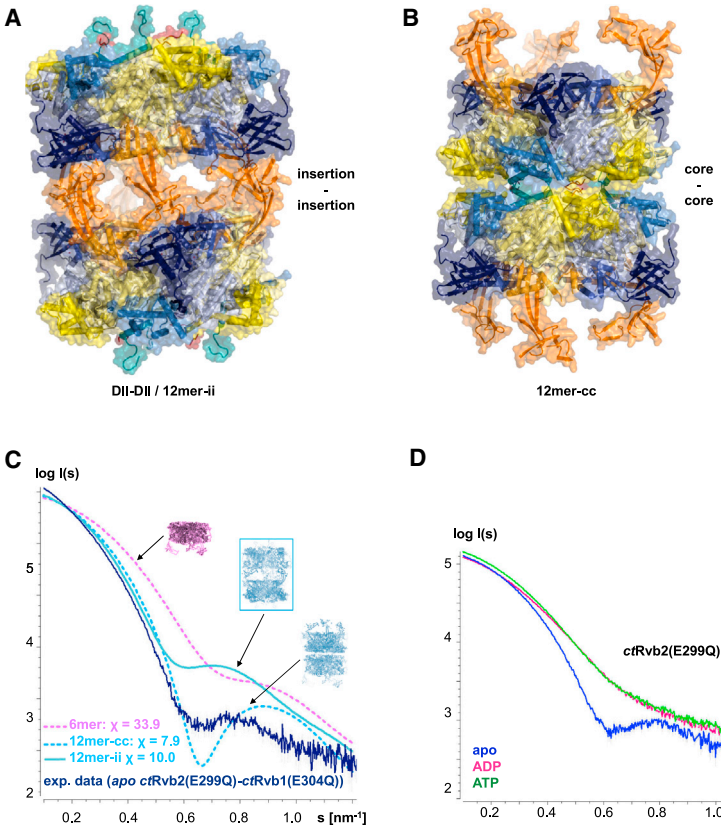

Figure 4. *Ct*Rvb1·*ct*Rvb2 Dodecamers

(A and B) Dodecameric assemblies in the crystal lattice. (A) DII-DII/insertion-insertion arrangement in which two hexamers interact via the DIIs of *ct*Rvb1 and *ct*Rvb2.

(B) Core-core assembly formed via the AAA+ cores.

(C) Experimental small-angle X-ray scattering (SAXS) data of *ct*Rvb2(E299Q)·*ct*Rvb1(E304Q) without added nucleotide (blue) in comparison with theoretical scattering curves of ADP-complex DII-DII (solid cyan line) or core-core (dashed cyan line) dodecamers or a hexamer (dashed violet line) and the corresponding chi values (χ) determined for the fit as a measure of discrepancy.

(D) SAXS curves of *ct*Rvb2(E299Q)·*ct*Rvb1(E304Q) in the presence of ADP or ATP, or without addition of any nucleotide (see also Figure S5B).

rings stack on top of each other. Two possible alternative stacking modes can be found in the crystal lattice (Figures 4A and 4B). According to the domains that form the main inter-ring interface, they are referred to as DII-DII for the insertion domains DII (12mer-ii) or core-core for the AAA+ core domains DI and DIII (12mer-cc). Both arrangements appear reasonable in the first place, since similar surface areas are buried (ca. 80,000 Å^2) relative to the overall surface (220,000 Å^2). The theoretic free energy values of disassembly ($\Delta G_{diss.}$) estimated for the two assemblies using PISA (Krissinel and Henrick, 2007) identified both potential assemblies as stable forms with the highest possible computed significance score of 1.0.

Small-Angle X-Ray Scattering Analysis of Dodecamer Assemblies

In general, small-angle X-ray scattering (SAXS) is a suitable tool to distinguish between models of different oligomerization nature. Here, it was used to determine which oligomer form matches the *ct*Rvb1·*ct*Rvb2 solution structure (Figure 4C). Yet the best fit was revealed for a mixture of DII-DII and core-core dodecamers populated with 63% and 37% (χ = 3.1) (see Supplemental Information for details).

Mutational Analysis of Dodecamer Formation

Two mutant complexes which either lack *ct*Rvb1's DII_{ext} or harbor a C-terminal GFP fusion at *ct*Rvb2 were analyzed by SEC. Both complexes eluted as dodecamers (with an additional minor fraction of oligomers as observed for the wild-type [WT] complex corresponding to a molecular weight of ca. 100 kDa).

Crosslinking Studies

Interaction surfaces of *ct*Rvb1·*ct*Rvb2 were mapped using a recently established approach that combines lysine-specific crosslinking with mass spectrometric analysis (XL-MS) (see Supplemental Experimental Procedures). Twenty-three *ct*Rvb1-*ct*Rvb2 inter-links fulfilling the quality criteria were obtained. Of these, 19 links can be explained by contacts within a single hexameric ring allowing no inference on the dodecamer's architecture. Yet the formation of the remaining four cross-links Lys163(*ct*Rvb1)-Lys156(*ct*Rvb2), Lys183(*ct*Rvb1)-Lys156 (*ct*Rvb2), Lys183(*ct*Rvb1)-Lys183(*ct*Rvb2), and Lys183(*ct*Rvb1)-Lys203(*ct*Rvb2) seems only reasonable in a DII-DII assembly. XL-MS data thus indicate the existence of the 12mer-ii form in solution. But it is particularly important to keep in mind that we just caught one rather stable conformation randomly in the crystal out of many "players" of a conformational ensemble, and that most likely several assembly forms coexist in solution as also suggested by the SAXS data.

Conserved Surfaces

Interestingly, the surface conservation of the *ct*Rvb1·*ct*Rvb2 hexamer is most prominent for the insertion domains and within the central channel (Figures 5 and S4A), while the top surface of the AAA+ domains is rather variable. One exception is a conserved patch which strikingly is largely covered by *ct*Rvb2's η2 in the ADP-complex, but widely accessible in the ATP-bound *ct*Rvb1/nucleotide-free *ct*Rvb2 state.

Inter-Ring Interactions of the DII-DII Assembly

EM studies on human and yeast Rvb1/Rvb2 mostly argue for the DII-DII architecture (Gribun et al., 2008; López-Perrote et al., 2012; Torreira et al., 2008). Our SAXS and XL-MS data suggest that such a DII-DII form also exists for *ct*Rvb1/*ct*Rvb2. The respective inter-ring interface III involves hydrogen bonds and nonbonded interactions (Table S2; Figures S3A and S3B). Via α5/α6 and the linker β strands, *ct*Rvb2 of one ring interacts with *ct*Rvb1 of the second ring at η2 and L8, which is stabilized in contrast to its (partially) disordered equivalent in *ct*Rvb2 (L9). It becomes clear that this residue stretch is rather flexible. Yet it

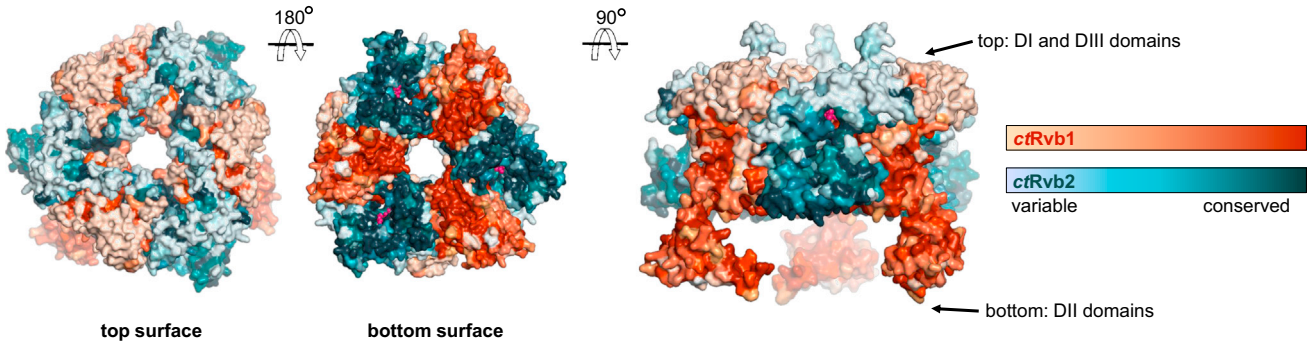

Figure 5. Surface Representation of the Hexamer Colored according to the Surface Conservation

The conservation is represented by different grades of red/orange or turquoise for *ct*Rvb1 and *ct*Rvb2, respectively, which gain more intense with increasing levels of conservation. From left to right: view onto the AAA+ core (DI/DIII), view onto DIIs, side view onto the exterior (see also Figures S4A–S4C).

obviously can be caught in a specific conformation, and this is likely dependent on interaction partners and is only visible in the ADP-complex. In contrast, the ATP/*apo* structure visualizes inter-ring interface IV consisting of two strictly conserved lysine residues (Lys183) of two *ct*Rvb1 molecules (Figure S3B; Table S2). The 12mer-ii and 12mer-cc forms might very well coexist and have distinct roles for specific functions. A mixture is in accordance with our SAXS data.

Inter-Ring Contacts in a Core-Core Dodecamer

Prominently, *ct*Rvb2's C-terminal α-hook interacts intimately with a highly conserved pocket of complementary shape on the top AAA+ core surface of the second ring (Figure S4B). These contacts are mainly hydrophobic, and *ct*Rvb1's C terminus protrudes from the side. The groove is located directly above *ct*Rvb2's ATP binding site (Figure S4C), and a connecting channel is blocked by the hook. According to in silico analyses with PISA (Krissinel and Henrick, 2007), the hook significantly contributes to the dodecamer's stability. Accordingly truncated ATP/*apo* or ADP-complexes yield 20% or even up to 60% lower ΔG_{diss} values. Therefore, we produced *ct*Rvb1·HisPP-*ct*Rvb2(Δ450–488) and *ct*Rvb1·HisPP-*ct*Rvb2(Δ435–488) complexes and determined their oligomeric states. Interestingly, SEC and native PAGE analyses suggest that both variants still can form dodecamers, yet minor fractions of hexameric species become obvious (Figure S4D).

ATPase Activity of *ct*Rvb1·*ct*Rvb2 WT and Mutant Complexes

To test the activity of the two distinct ATP binding sites in the complex, we examined the ATPase activity of *ct*Rvb1·*ct*Rvb2 WT and mutant complexes carrying single or double mutations of their Walker A (WA: *ct*Rvb1(K77L), *ct*Rvb2(K83L)) or Walker B (WB: *ct*Rvb1(E304Q), *ct*Rvb2(E299Q)) motifs. All mutants were purified as dodecamers (Figure S4D). *Ct*Rvb1·*ct*Rvb2 complexes have ATP hydrolysis activity at a temperature of 40°C but also 55°C, the optimal growth temperature of *C. thermophilum* (Figure 6). At a protein monomer concentration of 4 μM, the ATP hydrolysis rate has a turnover of ca. 3.0 mol ATP min^{-1} mol^{-1} protein monomer at 40°C and is increased to 8.5 ATP min^{-1} mol^{-1} at the elevated temperature. The Walker B double mutant complex was more or less inactive at both temperatures (2.6% or 1.9% of WT). The single Walker B mutants retained ca. 51% (R1WB-R2WT) or ca. 31% (R1WT-R2WB) activity at 40°C and even 81% (R1WB-R2WT) or ca. 73% (R1WT-R2WB) activity at 55°C. Under these conditions Rvb2 has a slightly stronger but very similar ATPase activity compared with Rvb1, although isolated Rvb1 appears to be more active than isolated Rvb2 (Gribun et al., 2008). Of note, the ATPase activities of both Rvb1 and Rvb2 within the complex seem to depend on the nucleotide binding state of the neighbor molecule. While slowing down ATP hydrolysis in the neighboring subunit via the Walker B mutant — and therefore stabilizing ATP in this subunit — only moderately reduces the overall activity of the complex, interfering with ATP binding by individual Walker A mutants more strongly reduces ATPase activity (to ca. 11% and 26% at 40°C or 11% and 2% at 55°C). In summary, slowing down or abolishing ATP hydrolysis in one subunit does not strongly affect the ATPase activity of the other subunit, while preventing ATP binding does. These data suggest that ATP binding to one subunit is required for ATPase activity in the other subunit.

Comparing Crystal Structures of *ct*Rvb1·*ct*Rvb2 ATP/*apo* and ADP-Complexes and Human Orthologs

As the available human *hs*Rvb1·*hs*Rvb2 structures (Figure S5C) have negligible root mean square deviations (rmsd) among each other, we chose the most complete, full-length *hs*Rvb1 structure (PDB ID 2C9O) (Matias et al., 2006) for further comparison (Figure 7A). Negligible rmsd values obtained from domain-wise comparison indicate that no significant structural changes are caused within the individual domains. The *ct*Rvb1·*ct*Rvb2 hexamer shares the dimensions and the flatness of the top surface with *hs*Rvb1 (outer diameter: 94–117 Å) (Matias et al., 2006), but its central channel is significantly wider (diameter of 25 Å versus 18 Å).

To assess conformational changes, the DIs of *ct*Rvb1/*ct*Rvb2 were superposed. The most prominent shift concerns DII (Figure 7A). In contrast, DIII's location is rather similar in ADP-bound *ct*Rvb1, *ct*Rvb2, and *hs*Rvb1, and no mentionable changes occur from ATP-bound to ADP-bound *ct*Rvb1. But, most importantly, DIII is shifted significantly between the ADP-bound and the nucleotide-free state of *ct*Rvb2. As the ring formation involves DI and DIII, this has an impact on the oligomerization architecture. Conformational changes between nucleotide-bound and nucleotide-free states, but minor variations in dependence

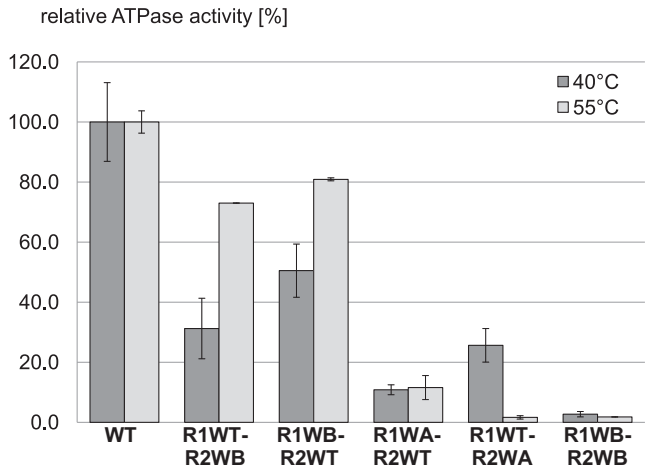

Figure 6. ATPase Activity Assays

ATPase activity of Walker A (WA) or Walker B (WB) mutant complexes of *ct*Rvb1 (R1) - *ct*Rvb2 (R2) complexes relative to the activity of the wild-type (WT) complex measured at the indicated temperatures.

Values were calculated from at least three replicates. Error bars represent standard deviations of the average values calculated using the *n*−*1* method ($\sqrt{\sum \frac{(x-\bar{x})^2}{(n-1)}}$ with sample mean *x* and sample size *n*).

on the nature of nucleotide, are corroborated by SAXS data (Figures 4D and S5B).

Comparison of *ct*Rvb1·*ct*Rvb2 ATP/*apo*- and ADP-Bound Dodecamers

Observed shifts between the ATP/*apo* and ADP-complexes are not caused by the crystal packing, as these are isomorphous. The intermolecular contacts at all interfaces differ between the ATP/*apo* and ADP-complex structures, but the most significant rearrangements concern the newly revealed inter-ring interface III (Figures 2 and 3). There are also positional alterations of specific subunits within the ring. This can be explained by breathing within monomers, particularly between DI and DIII and with regard to DII's position relative to them. For comparisons of the dodecameric ATP/*apo* and ADP-complex structures, DI of one *ct*Rvb1 molecule (chain A, marked by a gray background in Figure 7B) was taken as reference point for the structural alignment. The domain shifts between the ATP/*apo* and ADP-complex structures are minor for the molecules located in the same ring as the reference point, but huge in the second ring (indicated by arrows in the bottom left panel). Obviously, the effects are amplified here.

Comparison of *ct*Rvb1·*ct*Rvb2 with EM Structures of Human or Yeast Orthologs

As the two rings of the DII-DII *ct*Rvb1·*ct*Rvb2 dodecamer are related by a crystallographic symmetry element, they are identical. This is in contrast to the negative stain EM structure of the asymmetric *hs*Rvb1·*hs*Rvb2 dodecamer (Puri et al., 2007), which also deviates in the overall dimensions. Interestingly, their extent in width and length are interchanged: 118 Å diameter and 163–166 Å double-ring height for *ct*Rvb1·*ct*Rvb2 versus 158 Å diameter × 118 Å double-ring height (Puri et al., 2007), illustrating the extensive conformational flexibility of dodecamers. In contrast, the *ct*Rvb1·*ct*Rvb2 complex fits well to the overall dimensions and the AAA+ core layers of the compact conformation of the *hs*Rvb1·*hs*Rvb2 dodecamer (EMD-2163) (López-Perrote et al., 2012) (Figure 8A) or the *sc*Rvb1·*sc*Rvb2 dodecamer (EMD-2865) (Torreira et al., 2008) (Figure 8B). *Ct*Rvb1's and *ct*Rvb2's DIIs and the human counterparts occupy unequal places. This might be partially due to the 6-fold symmetry (D6) applied to process the EM data, preventing the discovery of differences between Rvb1 and Rvb2. Concerning the yeast complex, the locations of the DIIs also are in good agreement, though homo- rather than heterohexameric rings are assumed.

DISCUSSION

The Rvb1·Rvb2 complex is implicated in a large variety of biological contexts ranging from chromatin remodeling to PIKKs assembly and β-catenin-dependent oncogenic transformation. Besides the unresolved biochemical function of the Rvb1·Rvb2 complex in any of these contexts, the structures and functions of different oligomeric states, in particular the dodecamer form of the Rvb1·Rvb2 complex, need clarification. Here we report two full-length *ct*Rvb1·*ct*Rvb2 structures in different nucleotide binding states, allowing us to analyze the precise assembly geometry and its dynamic alteration by nucleotide binding. Interestingly, in contrast to 2D EM projections of yeast orthologs (Gribun et al., 2008), no significant differences in the overall dimensions are observed, although the crystal lattice interactions might prevent larger conformational changes between the different nucleotide states. Our crystal structures unambiguously show heterohexameric rings of alternating Rvb1 and Rvb2 and underline that two rings can build up a stable 2-fold symmetric dodecamer form.

The *ct*Rvb1·*ct*Rvb2 complex forms stable dodecamers in solution as demonstrated by SEC, static light scattering (SLS), SAXS, and XL-MS experiments and native PAGE (Figures 4C, 4D, S5A, and S5B; Table S3). This is consistent with AUC data on the human proteins (Niewiarowski et al., 2010). Two possible dodecamer forms can be assembled from adjacent hexameric rings in the crystal lattice. In one assembly, interactions are mediated by the DII insertion domains (12mer-ii), and in the other assembly by the AAA+ core domains (12mer-cc) (Figures 4A and 4B). XL-MS data indicate that the 12mer-ii form exists in solution. SAXS analyses suggest a mixture of 12mer-cc and 12mer-ii complexes (although they are complicated by transitions of DII around the DI-DII interdomain hinge regions and flexible loops). As the position of the characteristic DIIs relative to the AAA+ core of the described *ct*Rvb1·*ct*Rvb2 structures differs compared with other Rvb1·Rvb2 structures (Figures 7A and 8), they expand our insight into the conformational ensemble of different oligomeric domain arrangements (reviewed in Cheung et al., 2010a), which possibly reflect distinct functional states. Notably, the *ct*Rvb1·*ct*Rvb2 structures unveil additional intimate intra-ring contacts when compared with the mixed human complex (Gorynia et al., 2011) (Figures S3C, S3D, S5D, and S5E). Regions that were speculated to be involved in interactions with the second ring of the human dodecamer based on residual density patches form intra-ring contacts in the *ct*Rvb1·*ct*Rvb2 complexes instead. For *ct*Rvb1·*ct*Rvb2, only *ct*Rvb2's but not *ct*Rvb1's DII_{int} is involved in inter-ring contacts. Of note,

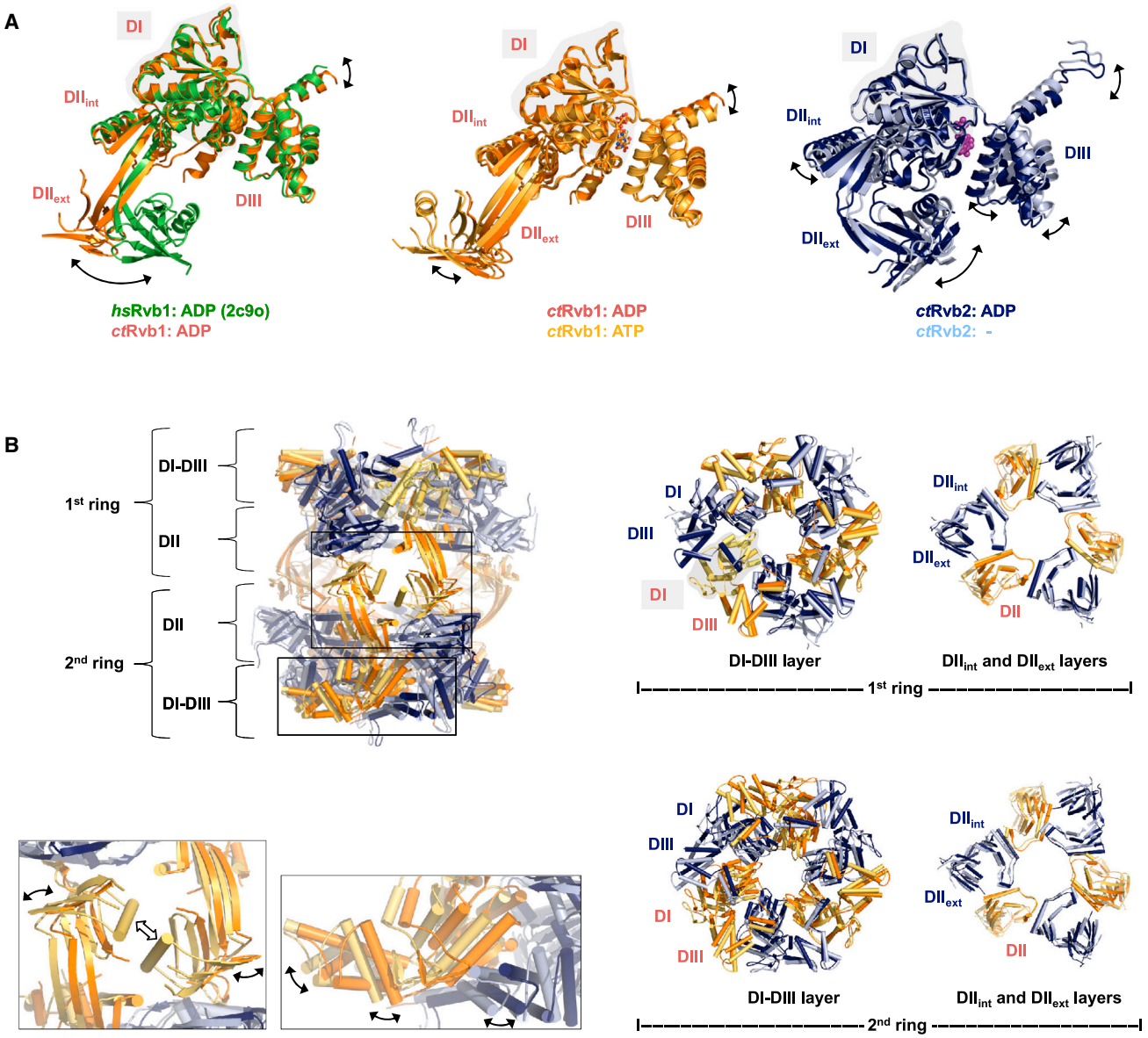

Figure 7. 3D Alignments of Structures in Distinct Nucleotide Binding States Based on DI (Gray Areas)

(A) *Hs*Rvb1, *ct*Rvb1, and *ct*Rvb2 monomers (see also Figure S5C).

(B) *Ct*Rvb1·*ct*Rvb2 DII-DII dodecamers. The top view representation is split into DI-DIII and DII planes separately for the upper and the bottom ring (see also Figure 2; Figures S3C, S3D, and S6).

homohexameric rings are also discussed with distinct interpretations concerning the nucleotide dependence (Gorynia et al., 2011; Matias et al., 2006; Niewiarowski et al., 2010; Puri et al., 2007). Thus, we do not exclude that hexamers or dodecamers of two homohexameric rings exist in specific macromolecular machines and are required in distinct physiological contexts.

The observed differences in DII positions among the compared structures are not surprising because of their enormous flexibility but are most probably of great functional relevance. DIIs are supposed to regulate ATP hydrolysis (Gorynia et al., 2011), and DII rearrangements drive conformational transitions between coexisting conformations and regulate the accessibility of DNA binding surfaces (López-Perrote et al., 2012). Rvb1's DII, which represents the presumable DNA binding region, occupies an unrevealed space and is involved in so far uncharacterized inter-ring interactions in our structures. Data on DNA binding are still controversial. The diameter of the central channel of the crystallized *ct*Rvb1·*ct*Rvb2 assemblies of 24–25 Å is clearly suited to enclose a double-stranded DNA substrate. And interestingly, potential nucleosome-binding interfaces cluster in Rvb1's DI area near DII and in Rvb2's DII (Figure S7B).

The purified and crystallized dodecameric *ct*Rvb1·*ct*Rvb2 complexes are active ATPases with a turnover of ca. 3.0–8.5 mol ATP min^{-1} mol^{-1} protein monomer at 40°–55°C. These

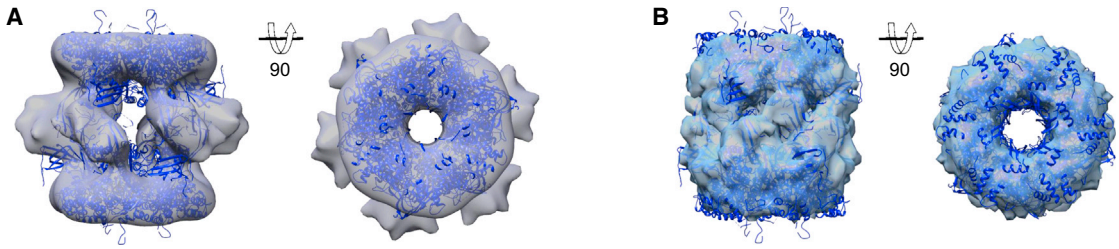

Figure 8. 3D Fitting of the Dodecameric DII-DII Crystal Structure of the *ct*Rvb1·*ct*Rvb2 ADP Complex into Electron Microscopy Envelopes
(A) Fit to the compact conformation of the *hs*Rvb1·hsRvb2 dodecamer (EMD-2163) (López-Perrote et al., 2012).
(B) Fit to the *S. cerevisiae* Rvb1·Rvb2 dodecamer (EMD-2865) (Torreira et al., 2008).

rates are comparable with those published for *Escherichia coli* RuvB (k_{cat} ~4.8) (Marrione and Cox, 1996) and the yeast Rvb1-Rvb2 complex (k_{cat} ~2.4) (Gribun et al., 2008). However, diverse factors will play regulatory roles in vivo as, e.g., recently shown for histone H3 amino-terminal tails that modulate the activity and oligomerization of orthologs from rat or human (Queval et al., 2014). Moreover, as described for other AAA+ ATPases, most likely also *ct*Rvb1·*ct*Rvb2 complexes couple ATP binding and hydrolysis to interdomain conformational rearrangements and asymmetry. Similar to the observations made in the *Thermotoga maritima* WT RuvB structure (PDB ID 1IN4) (Putnam et al., 2001), a misalignment of the Walker A and Walker B motif of both *ct*Rvb1 and *ct*Rv2 is seen in the ATP/*apo* structure. It is marked by the dissimilar distances from the Walker A lysine Cα to the Cα of the Walker B residues Asp303 (8.5 Å) and Glu304 (11.0 Å) or Asp298 (8.9 Å) and Glu299 (11.2 Å), respectively. The misalignment corresponds to a shift of α2 and α3 along the central β sheet of DI. Similar observations were also made in the ADP-complex, with Cα-Cα distances of 8.5 Å and 11.0 Å at *ct*Rvb1's active site or 8.8 Å and 10.9 Å for *ct*Rvb2. This conformation might explain why the BeF_3^- ion is not properly positioned and is thus not visible in the electron density. In any case, the ATPase mutant data suggest that ATP binding to one Rvb1 is needed to stimulate ATPase activity in Rvb2 and vice versa. The Walker A mutant data, showing that lack of binding to Rvb2 inhibits ATPase activity in Rvb1, nicely corresponds to the structural data, indicating that ATP bound to Rvb1 is not hydrolyzed when Rvb2's ATP binding site is empty. It remains unclear why we observe relatively homogeneous nucleotide occupancy with Rvb1's active site occupied by ATP and Rvb2's site empty, because from the ATPase data it is in principle also possible that ATP is stably bound at Rvb2 with Rvb1's site being empty. A likely explanation is that both ATP binding sites have significantly different affinities for ATP and are therefore functionally asymmetric.

While others found a significant influence of an N-terminal affinity tag at the Rvb1/Rvb2 proteins on the stabilization of the dodecamer (Cheung et al., 2010b), we observed only a negligible effect in SEC, SLS, and SAXS experiments (Figure S5A). Nevertheless, the N-terminal residue stretch of Rvb2 is well positioned to impact on oligomerization because it takes a course along interface II from the bottom of DII_{ext} to the ATP binding site, reaching it with η2. Although the tag itself is not visible in the *ct*Rvb1·*ct*Rvb2 structures, the conformation and anchorage of the N-terminal amino acids are correlated with the position of Rvb2's DII and interface II interactions. Interestingly, they depend on Rvb2's nucleotide binding state or vice versa. It is tempting to speculate that the N-terminal residues mimic the binding of protein interaction partners and their effects on oligomer state and architecture.

The observed interactions between *ct*Rvb2's C-terminal α-hook and the conserved groove on the AAA+ core top surface in a 12mer-cc assembly might represent an autoinhibitory state in vivo, as it is placed directly above *ct*Rvb2's ATP binding pocket (Figures S4B and S4C). Thus, it blocks a channel to the active site and might regulate the solvent accessibility for coeducts or products to enter or leave and, thereby, influence transitions between distinct states of the reaction pathway. In particular, due to possibilities of Rvb1 and Rvb2 to form oligomers of different composition and stoichiometry, such a regulated uptake and release of nucleotides would offer an enormous range of fine-tuning. It thus might affect cellular pathways and could be coordinated with the nutritional status of the cell, as currently discussed (Kakihara et al., 2014). *Ct*Rvb2's C-terminal extension (Arg448-Ser488) beyond α13 is not conserved in its entire length but is exclusively found in more closely related orthologs, e.g., from *Neurospora crassa*. Yet in species with shorter orthologs such as yeast or human, other molecules might exert such an inhibiting mechanism, e.g., peptide stretches of any interaction partner such as histone tails. Small molecules such as PI3P might be suitable candidates as well, since Rvb1/Rvb2 regulate the functions of PIKKs such as ATM and ATR and coordinate their activity (reviewed in Izumi et al., 2012). Notably, residues in Rvb2's C-terminal region are posttranslationally modified as a prerequisite for nuclear localization and repressive function in concert with β-catenin (Kim et al., 2006).

The experimentally determined structure of Rvb2's DII_{ext}, in particular revealing its unexpected sharply bent position, might help to further improve molecular dynamics (MD) simulations (Petukhov et al., 2012) that already paved the way to understand the molecular basis of the *liebeskummer* (*lik*) mutation. This Phe-Cys-Arg insertion in DII (between equivalents of Gly189 and Asp190 of *ct*Rvb2) (Figure S7C) finally results in heart failure and embryonic lethality (Rottbauer et al., 2002). In contrast to *lik*, Rvb2 mutations that lead to shortened telomeres (Grandin and Charbonneau, 2011) are located at domain interfaces

(Figure S7D). They will have a major impact on structural rearrangements, particularly those of DII_{int} during the ATP hydrolysis-ADP release cycle (Figure 7).

Rvb1 and Rvb2 are components of the chromatin remodeling complexes INO80 and SWR1 (Shen et al., 2000) and are required for INO80's structural and functional integrity (Jonsson et al., 2004). Crosslinking analysis of INO80 (Tosi et al., 2013) is consistent with the alternating hexamer and the dodecamer structure reported here, although the observed *ct*Rvb1·*ct*Rvb2 conformation is more elongated than INO80's head module (Tosi et al., 2013) which has been interpreted as an Rvb1·Rvb2 dodecamer. It is possible that contacts to other subunits of the INO80 complex (Figure S7A) promote a distinct conformation in Rvb1·Rvb2. In contrast, SWR1 appears to contain only a single hexameric Rvb1·Rvb2 ring (Nguyen et al., 2013). Understanding the nature of the different shapes and proposed oligomeric states of Rvb1·Rvb2 in related but distinct chromatin remodelers requires future studies on the basis of more highly resolved EM single-particle reconstructions.

Conclusions

The conserved AAA+ ATPases Rvb1 and Rvb2 are components of various macromolecular machines and are crucial for diverse cellular activities including cancer-related processes. Their controversially debated oligomeric structures and functions remain unclear. In summary, we report a structural framework for the assembly of Rvb1·Rvb2 oligomers in different nucleotide binding states, which provides a molecular basis for the functional analyses of Rvb1·Rvb2 hexamers or dodecamers in different cellular contexts. Strikingly, Rvb1's and Rvb2's characteristic OB folds occupy unequal positions. The conformational and positional flexibility of DIIs and the other domains will have a major impact on assembly and function, and the presence of Rvb2 in the hexameric ring provides new interdependent interactions between the DII and DI/DIII domains. Interestingly, the correlated positions of the Rvb1/Rvb2-specific insertion domains relative to the compact conserved AAA+ core ring are in agreement with predictions based on MD simulations (Afanasyeva et al., 2014; Petukhov et al., 2012). The structures uncover inter-ring interfaces with significant rearrangements between nucleotide-free and ATP-/ADP-bound states, highlighting Rvb1·Rvb2's conformational plasticity. They indicate nonconcerted ATPase activities and communication of functional roles by highly interconnected structural switches. Biochemical data indicate an interdependency of the two ATPase sites and that ATP binding, but not hydrolysis, in Rvb1 is a prerequisite for the ATPase activity of Rvb2 and vice versa.

EXPERIMENTAL PROCEDURES

Expression and Purification

Expression vectors encoding *C. thermophilum* Rvb1 and N-terminally His-tagged Rvb2 were generated using standard methods. The WT and Walker A or Walker B mutant proteins and truncated (*ct*Rvb1ΔDII$_{ext}$) or fusion (*ct*Rvb2-eGFP) proteins were coexpressed in *E. coli* Rosetta2(DE3) cells. They were purified in buffers containing 100–300 mM NaCl/5%–10% (v/v) glycerol/8–30 mM KHEPES/0–30 mM imidazole/3–5 mM β-mercaptoethanol pH 8.0 via Ni-NTA affinity, anion-exchange chromatography, and SEC, and concentrated to up to 8 mg/ml. Full details can be found in the Supplemental Experimental Procedures.

Crystallization, Data Collection, and Structure Determination

Crystallization was performed using sitting drop vapor diffusion against 1 M sodium malonate pH 6.0 at 20°C without addition of any nucleotide or after preincubation with an ADP-BeF_3 mix. Hexagonal crystals of space group R32 were soaked in cryo buffer and flash-cooled. X-ray diffraction data of single crystals were collected on beamlines PX I (X06SA; Swiss Light Source, Villingen, Switzerland) or ID29 (ESRF, France) at 100 K. The structures were determined using molecular replacement with domains I and III of human RuvBL1 (PBD ID 2c9o) (Matias et al., 2006) as search model and refined to a resolution of 3.6 Å (ATP/*apo* structure) or 2.9 Å (ADP-complex structure) as outlined in detail in the Supplemental Information. Images were generated using PyMol (The PyMOL Molecular Graphics System, Version 1.2r3pre. Schrödinger, LLC) and Chimera (Pettersen et al., 2004). In accordance with Matias et al. (2006), the diameter of the central channel (Figures 1D and 1E) was measured between Asp343 of *ct*Rvb1 and Thr337 of the opposite *ct*Rvb2.

Crosslinking and Mass Spectrometry

Monodisperse *ct*Rvb1·His8PP*ct*Rvb2 was crosslinked with an equimolar mixture of isotopically light and heavy labeled disuccinimidyl suberate. The crosslinked complex was purified by SEC prior to preparation of crosslinked peptides for liquid chromatography-tandem mass spectrometry analysis. Only distances below 35 Å were considered. Details are described in Supplemental Experimental Procedures.

SAXS

SAXS data were collected at beamlines X33 or P12, EMBL/DESY (Hamburg, Germany) at 10°C and analyzed using the ATSAS package (Petoukhov et al., 2012) as outlined in Supplemental Experimental Procedures. Different concentrations of WT and Walker B mutant proteins with His_8PP tag and without any tag, without addition of any nucleotide or in the presence of ATP, ADP, AMPPcP, or ATPγS, were tested in batch analyses. Representative samples were subjected to an online fast protein liquid chromatography separation system immediately before data collection, proving the high quality and monodispersity of the samples.

ATPase Activity Assay

ATPase reactions were carried out at 40°C, and the release of inorganic phosphate was monitored at 22°C by using the EnzChek phosphate assay Kit (Invitrogen) as described in the Supplemental Information. The Walker B double mutant complex *ct*Rvb1(E304Q)·*ct*Rvb2(E299Q) (purified using the same protocol) served as negative control (background ATPase activity: 0.08 or 0.16 mol ATP min^{-1} mol^{-1} monomer at 40°C or 55°C, respectively). The Walker A double mutant complex *ct*Rvb1(K77L)·*ct*Rvb2(K83L) unexpectedly exhibited an activity with a k_{cat} of 0.94 mol ATP min^{-1} mol^{-1} monomer at 40°C. According to SDS-PAGE analysis, this sample was contaminated with an additional band likely representing a chaperone. Activity was negligible at 55°C, a temperature at which most proteins from the expression host are rather inactive.

ACCESSION NUMBERS

The PDB accession numbers for the refined structures reported in this paper are 4WVY (ATP/*apo* complex) and 4WW4 (ADP-complex).

SUPPLEMENTAL INFORMATION

Supplemental Information includes seven figures, three tables, and Supplemental Experimental Procedures and can be found with this article online at http://dx.doi.org/10.1016/j.str.2014.12.015.

ACKNOWLEDGMENTS

We thank the Max-Planck Crystallisation Facility, Martinsried, Germany and the staff at the beamlines PX I (X06SA) of SLS and ID29 of ESRF for support during synchrotron data collection. We are grateful to Brigitte Kessler and Manuela Moldt for excellent technical support and to Klaus Förstemann, Sebastian Eustermann, and Gregor Witte for valuable discussions. This work was supported by the Collaborative Research Center 1064, the Center for

Integrated Protein Science Munich, the Graduate Research and Training Network 1721 of the German Research Council, and ERC Advanced Grant (ATMMACHINE) to K.-P.H.

Received: August 11, 2014
Revised: November 14, 2014
Accepted: December 11, 2014
Published: February 5, 2015

REFERENCES

Afanasyeva, A., Hirtreiter, A., Schreiber, A., Grohmann, D., Pobegalov, G., McKay, A.R., Tsaneva, I., Petukhov, M., Kas, E., Grigoriev, M., and Werner, F. (2014). Lytic water dynamics reveal evolutionarily conserved mechanisms of ATP hydrolysis by TIP49 AAA+ ATPases. Structure *22*, 549–559.

Ammelburg, M., Frickey, T., and Lupas, A.N. (2006). Classification of AAA+ proteins. J. Struct. Biol. *156*, 2–11.

Chen, L., Conaway, R.C., and Conaway, J.W. (2013). Multiple modes of regulation of the human Ino80 SNF2 ATPase by subunits of the INO80 chromatin-remodeling complex. Proc. Natl. Acad. Sci. USA *110*, 20497–20502.

Cheung, K.L., Huen, J., Houry, W.A., and Ortega, J. (2010a). Comparison of the multiple oligomeric structures observed for the Rvb1 and Rvb2 proteins. Biochem. Cell Biol. *88*, 77–88.

Cheung, K.L., Huen, J., Kakihara, Y., Houry, W.A., and Ortega, J. (2010b). Alternative oligomeric states of the yeast Rvb1/Rvb2 complex induced by histidine tags. J. Mol. Biol. *404*, 478–492.

Gorynia, S., Bandeiras, T.M., Pinho, F.G., McVey, C.E., Vonrhein, C., Round, A., Svergun, D.I., Donner, P., Matias, P.M., and Carrondo, M.A. (2011). Structural and functional insights into a dodecameric molecular machine—the RuvBL1/RuvBL2 complex. J. Struct. Biol. *176*, 279–291.

Grandin, N., and Charbonneau, M. (2011). Rvb2/reptin physically associates with telomerase in budding yeast. FEBS Lett. *585*, 3890–3897.

Gribun, A., Cheung, K.L., Huen, J., Ortega, J., and Houry, W.A. (2008). Yeast Rvb1 and Rvb2 are ATP-dependent DNA helicases that form a heterohexameric complex. J. Mol. Biol. *376*, 1320–1333.

Huber, O., Menard, L., Haurie, V., Nicou, A., Taras, D., and Rosenbaum, J. (2008). Pontin and reptin, two related ATPases with multiple roles in cancer. Cancer Res. *68*, 6873–6876.

Huen, J., Kakihara, Y., Ugwu, F., Cheung, K.L., Ortega, J., and Houry, W.A. (2010). Rvb1-Rvb2: essential ATP-dependent helicases for critical complexes. Biochem. Cell Biol. *88*, 29–40.

Ikura, T., Ogryzko, V.V., Grigoriev, M., Groisman, R., Wang, J., Horikoshi, M., Scully, R., Qin, J., and Nakatani, Y. (2000). Involvement of the TIP60 histone acetylase complex in DNA repair and apoptosis. Cell *102*, 463–473.

Izumi, N., Yamashita, A., and Ohno, S. (2012). Integrated regulation of PIKK-mediated stress responses by AAA+ proteins RUVBL1 and RUVBL2. Nucleus *3*, 29–43.

Jha, S., and Dutta, A. (2009). RVB1/RVB2: running rings around molecular biology. Mol. Cell *34*, 521–533.

Jonsson, Z.O., Jha, S., Wohlschlegel, J.A., and Dutta, A. (2004). Rvb1p/Rvb2p recruit Arp5p and assemble a functional Ino80 chromatin remodeling complex. Mol. Cell *16*, 465–477.

Kakihara, Y., and Houry, W.A. (2012). The R2TP complex: discovery and functions. Biochim. Biophys. Acta *1823*, 101–107.

Kakihara, Y., Makhnevych, T., Zhao, L., Tang, W., and Houry, W.A. (2014). Nutritional status modulates box C/D snoRNP biogenesis by regulated subcellular relocalization of the R2TP complex. Genome Biol. *15*, 404.

Kanemaki, M., Kurokawa, Y., Matsu-ura, T., Makino, Y., Masani, A., Okazaki, K., Morishita, T., and Tamura, T.A. (1999). TIP49b, a new RuvB-like DNA helicase, is included in a complex together with another RuvB-like DNA helicase, TIP49a. J. Biol. Chem. *274*, 22437–22444.

Kim, J.H., Choi, H.J., Kim, B., Kim, M.H., Lee, J.M., Kim, I.S., Lee, M.H., Choi, S.J., Kim, K.I., Kim, S.I., et al. (2006). Roles of sumoylation of a reptin chromatin-remodelling complex in cancer metastasis. Nat. Cell Biol. *8*, 631–639.

King, T.H., Decatur, W.A., Bertrand, E., Maxwell, E.S., and Fournier, M.J. (2001). A well-connected and conserved nucleoplasmic helicase is required for production of box C/D and H/ACA snoRNAs and localization of snoRNP proteins. Mol. Cell Biol. *21*, 7731–7746.

Krissinel, E., and Henrick, K. (2007). Inference of macromolecular assemblies from crystalline state. J. Mol. Biol. *372*, 774–797.

Krogan, N.J., Keogh, M.C., Datta, N., Sawa, C., Ryan, O.W., Ding, H., Haw, R.A., Pootoolal, J., Tong, A., Canadien, V., et al. (2003). A Snf2 family ATPase complex required for recruitment of the histone H2A variant Htz1. Mol. Cell *12*, 1565–1576.

López-Perrote, A., Muñoz-Hernández, H., Gil, D., and Llorca, O. (2012). Conformational transitions regulate the exposure of a DNA-binding domain in the RuvBL1-RuvBL2 complex. Nucleic Acids Res. *40*, 11086–11099.

López-Perrote, A., Alatwi, H.E., Torreira, E., Ismail, A., Ayora, S., Downs, J.A., and Llorca, O. (2014). Structure of Yin Yang 1 oligomers that cooperate with RuvBL1-RuvBL2 ATPases. J. Biol. Chem. *289*, 22614–22629.

Makino, Y., Kanemaki, M., Kurokawa, Y., Koji, T., and Tamura, T. (1999). A rat RuvB-like protein, TIP49a, is a germ cell-enriched novel DNA helicase. J. Biol. Chem. *274*, 15329–15335.

Marrione, P.E., and Cox, M.M. (1996). Allosteric effects of RuvA protein, ATP, and DNA on RuvB protein-mediated ATP hydrolysis. Biochemistry *35*, 11228–11238.

Matias, P.M., Gorynia, S., Donner, P., and Carrondo, M.A. (2006). Crystal structure of the human AAA+ protein RuvBL1. J. Biol. Chem. *281*, 38918–38929.

Nano, N., and Houry, W.A. (2013). Chaperone-like activity of the AAA+ proteins Rvb1 and Rvb2 in the assembly of various complexes. Philos. Trans. R. Soc. Lond. B. Biol. Sci. *368*, 20110399.

Nguyen, V.Q., Ranjan, A., Stengel, F., Wei, D., Aebersold, R., Wu, C., and Leschziner, A.E. (2013). Molecular architecture of the ATP-dependent chromatin-remodeling complex SWR1. Cell *154*, 1220–1231.

Niewiarowski, A., Bradley, A.S., Gor, J., McKay, A.R., Perkins, S.J., and Tsaneva, I.R. (2010). Oligomeric assembly and interactions within the human RuvB-like RuvBL1 and RuvBL2 complexes. Biochem. J. *429*, 113–125.

Papin, C., Humbert, O., Kalashnikova, A., Eckert, K., Morera, S., Kas, E., and Grigoriev, M. (2010). 3'- to 5' DNA unwinding by TIP49b proteins. FEBS J. *277*, 2705–2714.

Petoukhov, M.V., Franke, D., Shkumatov, A.V., Tria, G., Kikhney, A.G., Gajda, M., Gorba, C., Mertens, H.D.T., Konarev, P.V., and Svergun, D.I. (2012). New developments in the ATSAS program package for small-angle scattering data analysis. J. Appl. Crystallogr. *45*, 342–350.

Pettersen, E.F., Goddard, T.D., Huang, C.C., Couch, G.S., Greenblatt, D.M., Meng, E.C., and Ferrin, T.E. (2004). UCSF Chimera—a visualization system for exploratory research and analysis. J. Comput. Chem. *25*, 1605–1612.

Petukhov, M., Dagkessamanskaja, A., Bommer, M., Barrett, T., Tsaneva, I., Yakimov, A., Queval, R., Shvetsov, A., Khodorkovskiy, M., Kas, E., and Grigoriev, M. (2012). Large-scale conformational flexibility determines the properties of AAA+ TIP49 ATPases. Structure *20*, 1321–1331.

Puri, T., Wendler, P., Sigala, B., Saibil, H., and Tsaneva, I.R. (2007). Dodecameric structure and ATPase activity of the human TIP48/TIP49 complex. J. Mol. Biol. *366*, 179–192.

Putnam, C.D., Clancy, S.B., Tsuruta, H., Gonzalez, S., Wetmur, J.G., and Tainer, J.A. (2001). Structure and mechanism of the RuvB Holliday junction branch migration motor. J. Mol. Biol. *311*, 297–310.

Queval, R., Papin, C., Dalvai, M., Bystricky, K., and Humbert, O. (2014). Reptin and Pontin oligomerization and activity are modulated through histone H3 amino-terminal tail interaction. J. Biol. Chem. *289*, 33999–34012.

Rosenbaum, J., Baek, S.H., Dutta, A., Houry, W.A., Huber, O., Hupp, T.R., and Matias, P.M. (2013). The emergence of the conserved AAA+ ATPases Pontin and Reptin on the signaling landscape. Sci. Signal *6*, mr1.

Rottbauer, W., Saurin, A.J., Lickert, H., Shen, X., Burns, C.G., Wo, Z.G., Kemler, R., Kingston, R., Wu, C., and Fishman, M. (2002). Reptin and pontin antagonistically regulate heart growth in zebrafish embryos. Cell *111*, 661–672.

Shen, X., Mizuguchi, G., Hamiche, A., and Wu, C. (2000). A chromatin remodelling complex involved in transcription and DNA processing. Nature *406*, 541–544.

Snider, J., and Houry, W.A. (2008). AAA+ proteins: diversity in function, similarity in structure. Biochem. Soc. Trans. *36*, 72–77.

Torreira, E., Jha, S., Lopez-Blanco, J.R., Arias-Palomo, E., Chacon, P., Canas, C., Ayora, S., Dutta, A., and Llorca, O. (2008). Architecture of the pontin/reptin complex, essential in the assembly of several macromolecular complexes. Structure *16*, 1511–1520.

Tosi, A., Haas, C., Herzog, F., Gilmozzi, A., Berninghausen, O., Ungewickell, C., Gerhold, C.B., Lakomek, K., Aebersold, R., Beckmann, R., and Hopfner, K.P. (2013). Structure and subunit topology of the INO80 chromatin remodeler and its nucleosome complex. Cell *154*, 1207–1219.

Venteicher, A.S., Meng, Z., Mason, P.J., Veenstra, T.D., and Artandi, S.E. (2008). Identification of ATPases pontin and reptin as telomerase components essential for holoenzyme assembly. Cell *132*, 945–957.

Wendler, P., Ciniawsky, S., Kock, M., and Kube, S. (2012). Structure and function of the AAA+ nucleotide binding pocket. Biochim. Biophys. Acta *1823*, 2–14.